

# Tunable Topological Dirac Surface States and Van Hove Singularities in Kagome Metal GdV<sub>6</sub>Sn<sub>6</sub>

**Yong Hu** (✉ [yonghphysics@gmail.com](mailto:yonghphysics@gmail.com))

Paul Scherrer Institut <https://orcid.org/0000-0002-4997-4143>

**Xianxin Wu**

Max-Planck-Institut

**Yongqi Yang**

Rutgers University

**Nicholas Plumb**

Paul Scherrer Institut <https://orcid.org/0000-0002-2334-8494>

**Andreas Schnyder**

Max Planck Institute for Solid State Research <https://orcid.org/0000-0002-1029-815X>

**Weiwei Xie**

Rutgers University

**Junzhang Ma**

City University of Hong Kong <https://orcid.org/0000-0002-4648-3576>

**Ming Shi**

Paul Scherrer Institute <https://orcid.org/0000-0002-6090-8219>

---

## Article

### Keywords:

**Posted Date:** April 14th, 2022

**DOI:** <https://doi.org/10.21203/rs.3.rs-1529357/v1>

**License:**  This work is licensed under a Creative Commons Attribution 4.0 International License. [Read Full License](#)

---

## Abstract

Realizing and tuning novel electronic states is of great interest and importance to modern condensed-matter physics and spintronics applications. Transition-metal-based kagome materials are a rich frontier for the investigation of novel topological electronic states and correlated phenomena. The divergent density of states in the kagome lattice due to van Hove singularities (VHSs) in the vicinity of the Fermi level (EF) also provide an ideal playground for the search of exotic correlated quantum states on a kagome lattice. However, in the idealized two-dimensional kagome lattice, topologically non-trivial Dirac surface states (TDSSs) have not been unambiguously observed, and the manipulation of TDSSs and VHSs remains largely unexplored. Here, combining angle-resolved photoemission spectroscopy with density functional theory calculations, we clearly reveal TDSSs originating from a  $\mathbb{Z}_2$  bulk topology for the first time in kagome lattices and identify two types of VHSs near EF in a newly discovered magnetic kagome material, GdV<sub>6</sub>Sn<sub>6</sub>. Remarkably, using in-situ surface potassium deposition to elevate carrier density, we successfully realize manipulation of the TDSSs and VHSs. The Dirac point of the TDSSs can be tuned from above to below EF, which reverses the chirality of the spin texture at the Fermi surface. These results not only establish GdV<sub>6</sub>Sn<sub>6</sub> as a fascinating platform for studying the nontrivial band topology, magnetism and correlation effects native to kagome lattices, but also open up a new avenue for the potential application of spintronic devices based on kagome materials.

## Main Text

The exploration of topological physics intertwined with non-trivial lattice geometries and strong electron interactions is emerging as a new frontier in condensed-matter physics [1-27]. Transition-metal-based kagome lattices, owing to the unique lattice geometry, have attracted particular attention, as they often show correlated topological band structures, magnetism, and diverse exotic electronic instabilities, such as spin liquid states, charge density wave (CDW), and superconductivity [1-9]. Recently, a number of experimental efforts have investigated topological phenomena in transition-metal-based kagome magnets, such as Fe<sub>3</sub>Sn<sub>3</sub> [3], FeSn [7], Co<sub>3</sub>Sn<sub>2</sub>S<sub>2</sub> [4,11,12], and RMn<sub>6</sub>Sn<sub>6</sub> (where R is a rare-earth element, and the kagome layers are made of manganese atoms) [8,13-15]. In particular, the topological surface states derived from relativistic Weyl points, namely surface Fermi arcs, have been observed in the time-reversal symmetry-broken Weyl semimetal Co<sub>3</sub>Sn<sub>2</sub>S<sub>2</sub> with ferromagnetism [11,12]. In addition, various forms of magnetism in the low-temperature electronic ground state enable the realization of quantum-limit Chern topological magnetism [8]. Besides these intensively studied magnetic kagome materials, the recently discovered non-magnetic kagome metals AV<sub>3</sub>Sb<sub>5</sub> (A=K, Rb, Cs) were found to possess a unique combination of novel correlated phenomena and nontrivial band topology [9,10,16-20]. An intriguing chiral CDW instability [21,22] and superconductivity [10,16,17] have been observed in the absence of magnetic orders, suggesting that the vanadium kagome lattice is an ideal platform for investigating correlated quantum states. Moreover, Dirac nodal lines and nodal loops have been identified in the non-magnetic kagome metal CsV<sub>3</sub>Sb<sub>5</sub> [23]. Apart from various types of topological band crossings (e.g., Dirac and Weyl fermions),  $\mathbb{Z}_2$  topology in kagome materials has also been proposed by theoretical calculations [16]; however, identifying and confirming the corresponding topological nature of surface states have remained an outstanding challenge, due to the lack of good candidate systems. Therefore, no clear experimental evidence for the  $\mathbb{Z}_2$  topological Dirac surface states (TDSSs) in kagome materials has been reported to date. For instance, the expected topological surface states (TSSs) in CsV<sub>3</sub>Sb<sub>5</sub> from density functional theory (DFT) calculations lie above the Fermi level ( $E_F$ ) and mostly overlap with the projection of bulk states [16,24]. Moreover, it has remained unclear how these kagome surface states could be manipulated, a key question relevant for potential applications.

GdV<sub>6</sub>Sn<sub>6</sub> is a newly discovered kagome system that exhibits a magnetic transition at a low temperature  $T_m \sim 5$  K [25,26]. In contrast to other members of the kagome magnet family, it is the Gd-triangular lattice that generates magnetism, while the kagome layer composed of V and Sn atoms is non-magnetic (Fig. 1a). The separation of the magnetic layer and kagome layer not only permits a direct study of the electronic structure of non-magnetic kagome layer but also introduces a magnetic tunability from the magnetic layer below  $T_m$ . Band structure calculations suggest that GdV<sub>6</sub>Sn<sub>6</sub> is topologically nontrivial, characterized by a  $\mathbb{Z}_2$  topological invariant in the paramagnetic state [25]. In contrast to other  $\mathbb{Z}_2$  kagome metals, such as CsV<sub>3</sub>Sb<sub>5</sub>, GdV<sub>6</sub>Sn<sub>6</sub> has a large bulk gap around G, allowing the TDSSs to be well separated from bulk states around the surface Brillouin zone (BZ) center (G point) (as illustrated in Fig. 1b). Therefore, GdV<sub>6</sub>Sn<sub>6</sub> is a tantalizing system to access and tune TDSSs, which is crucial for exploring potential applications in spintronics. Moreover, multiple van Hove singularities (VHSs), originating from the vanadium *d* orbitals appear near the  $E_F$  at the

*M* points (Fig. 1c), providing a promising playground for the search of exotic or related states on the kagome lattice. Whether or not the predicted non-trivial *M* points at van Hove filling in GdV<sub>6</sub>Sn<sub>6</sub>, the existence of the TDSSs – as well as the manipulation of the TDSSs and VHSs – in kagome metals have yet to be experimentally demonstrated.

In this work, via a combination of angle-resolved photoemission spectroscopy (ARPES) and DFT calculations, we unambiguously reveal the characteristic  $\mathbb{Z}_2$  TDSSs for the first time in kagome lattices and identify two types (*p*-type and *m*-type) of VHSs at the *M* points, in the paramagnetic phase of the magnetic kagome metal GdV<sub>6</sub>Sn<sub>6</sub>. Remarkably, the direct manipulation of the TDSSs and VHSs is realized by surface potassium deposition, where the Dirac point of the TDSSs shifts from above to below the  $E_F$  with increasing electron doping. The direct identification of surface states, combined with the spin texture from theoretical calculations, confirms the bulk nontrivial  $\mathbb{Z}_2$  topology and shows great promise for realizing spin polarization reversal on the surface Fermi surfaces in GdV<sub>6</sub>Sn<sub>6</sub>. Our observation of tunable correlated and topological electronic states not only establishes GdV<sub>6</sub>Sn<sub>6</sub> as a fertile system for exploring the interplay between the nontrivial band topology, magnetism, and correlation effects native to kagome lattices, but also unlocks new perspectives for the realization of spintronic devices based on kagome materials.

GdV<sub>6</sub>Sn<sub>6</sub> has a layered crystal structure with the space group P6/mmm and hexagonal lattice constants  $a = 5.5 \text{ \AA}$  and  $c = 9.2 \text{ \AA}$ . It consists of V<sub>3</sub>Sn kagome layers with Sn and GdSn<sub>2</sub> layers successively distributed in alternating layers stacked along the  $c$  axis [Figs. 1a(i) and (ii)] [25]. From the crystal structure, we find that chemical bonding between V<sub>3</sub>Sn and Sn layers is strong while the bonding between the V<sub>3</sub>Sn and GdSn<sub>2</sub> layers is weaker. Therefore, cleaving the crystal along (001) direction will result in two possible surface terminations, namely the V kagome and GdSn<sub>2</sub> terminations marked as V layer and GdSn<sub>2</sub> layer in Fig. 1a(iii). Figure 1d illustrates the bulk BZ and the projected two-dimensional (001) surface BZ, with high-symmetry points indicated. The band structure of GdV<sub>6</sub>Sn<sub>6</sub> in the paramagnetic phase from DFT calculations is displayed in Fig. 1e, where four VHS points emerge at the M in the vicinity of  $E_F$  (indicated by the red arrows and labeled as VHS1-4). A closer examination of the orbitally decomposed electronic structure from DFT indicates that the states of VHS1, VHS2 and VHS3 at the M point, characterized by V  $d_{xz}$ ,  $d_{xy}$  and  $d_{z^2}$  orbitals, are solely attributed to one sublattice in the V kagome lattice, and thus are of  $p$ -type [19,20,27]. In contrast, the states of VHS4 at the M point are attributed to a mixture of two sublattices, and thus are of  $m$ -type (for details, see Supplementary S1). Interestingly, along the K-M direction, the  $p$ -type VHS1 and VHS2 bands disperse with the opposite sign compared to the VHS3 bands, which is attributed to the sign change of the hopping parameters of  $d_{xz}$  and  $d_{xy}$  orbitals. The continuous direct gaps between bands appearing at every  $k$  point allow one to define the  $\mathbb{Z}_2$  topological invariant for the occupied bands using parity products at time-reversal invariant momenta [28]. Consistent with previous calculations [25], a strong topological invariant  $\mathbb{Z}_2 = 1$  is assigned to bands 171 (green) and 169 (blue), while the topmost band 173 (red) is topologically trivial. Owing to the band inversion around the A point for the 172 occupied bands, Dirac-cone-like TSSs are expected to reside in the large local band gap at G (Supplementary Fig. S2). Motivated by these theoretical observations, we employ ARPES to systematically study the topological electronic structures of single-crystal GdV<sub>6</sub>Sn<sub>6</sub>.

Due to the two possible surface terminations upon cleaving [Fig. 1a(iii)], we expect to observe two different types of ARPES spectra [29]. By using a small beam spot and measuring the Sn  $4d$  core level, we have resolved the two types of terminations on the cleaved sample surface and probed their electronic structures separately. Figure 2 summarizes the photoemission experiments on pristine, freshly cleaved GdV<sub>6</sub>Sn<sub>6</sub>.

We first focus on the electronic structure from the kagome termination (see Supplementary Fig. S3 for a detailed description of the termination assignments). The corresponding X-ray photoelectron spectroscopy (XPS) spectrum on the Sn  $4d$  core level and Fermi surface (FS) are shown in Figs. 2a and 2b, respectively (also see Fig. S3). Photon energy-dependent ARPES measurements on the kagome V layer along two different high-symmetry paths, i.e., the  $G - K - M - K$  (compare Figs. 2c and 2e) and  $G - M - G$  (see Figs. 2d and 2f) directions, exhibit distinct band dispersions at different  $k_z$  planes, indicating the three-dimensionality of the electronic structure in GdV<sub>6</sub>Sn<sub>6</sub> (consistent with the calculations in Fig. 1e). Similar to other kagome lattices, the characteristic Dirac cone around the  $Kp\phi$  and the  $VHSp\phi \neq arM$  of the kagome lattice are observed on the kagome termination (see Supplementary Figs. S4).

The APRES spectra collected on the GdSn<sub>2</sub> termination, shown in Figs. 2g-2j, is even richer than that on the kagome termination. The XPS spectrum on the Sn core level and FS from the GdSn<sub>2</sub> layer are plotted in Figs. 2g and 2h, respectively. The most prominent features of the FS (Fig. 2h) are the circular-shaped pocket near the BZ center ( $Gp\phi$ , highlighted by the dashed  $\circ \leq \in$  Fig. 2h) and the  $ahexagonal$ -shaped sheet ( $dashedhexagon \in$  Fig. 2h). The  $b$  and  $d$  dispers  $G$  point (Fig. 2j) further reveals that the circular- and hexagonal-shaped Fermi surfaces are formed by two V-shaped bands (highlighted by the red box in Fig. 2j). In addition, the measured dispersions uncover an electron-like band (centered at M) along the  $G - K - M - K$  direction (Fig. 2i) and a hole-like band along the  $G - M - G$  direction (Fig. 2j),  $c \leq arlyexhibit \in gasadd \leq p\phi$  at the M point (Fig. 2k), indicating the presence of a VHS, as sketched in Fig. 1c. A careful comparison (see Supplementary Fig. S5) between the experimental and calculated bands shows good overall agreement, and indicates that the identified VHS corresponds to the VHS1 labeled in Fig. 1e. On the other hand, the observed double V-shaped bands around the  $G$  point appear within the bulk band gap (Fig. 1e), implying the presence of surface states on the kagome metals GdV<sub>6</sub>Sn<sub>6</sub>.

To further validate the surface nature of double V-shaped bands around the  $G$  point, we have conducted photon energy-dependent ARPES measurement. Photoemission spectra recorded at various photon energies from 40 to 100 eV reveal that the V-shaped bands around  $G$  do not disperse with respect to photon energy (and thus  $k_z$ ), in contrast to the bulk states (for details, see Supplementary Fig. S6). The  $k_z$  independence of the V-shaped bands, as illustrated by two representative spectra taken with 76 eV and 86 eV in Fig. 3a, confirms the two-dimensional nature of the discussed surface bands. To further explore the topological nature of the surface states, we plot in Figs. 3b and 3c the calculated bulk states projected onto the (001) surface together with the theoretical surface spectra for the GdSn<sub>2</sub> termination (also see Supplementary Fig. S7). Comparing the measurements (Fig. 3a) with the theory calculations (Figs. 3b and 3c), the TSSs derived from bulk nontrivial topology can be clearly identified around the  $Gp\phi$  ( $\in dicatedbytheblackarrows \in$  Fig. 3c). Notably, the  $b$ -by- $s$  comparison of the  $b$  and  $d$  dispersion along the  $G - M$  direction (Figs. 3a and 3d) and the evolution of constant energy contours at different binding energies (Figs. 3e and 3f) show excellent agreement, suggesting that the observed surface states are derived from the bulk nontrivial  $\mathbb{Z}_2$  topology in kagome metals.

After the identification of the TSSs and VHS bands, we further demonstrate their manipulation via *in-situ* surface potassium deposition. The accumulation of the K atoms on the sample surface can be seen by measuring the K 3*p* core level, which is absent on the pristine surface (blue curve in Fig. 4a), but grows in intensity with the surface deposition (purple and red curves in Fig. 4a). With increasing doping, the Dirac point of the TSSs is tuned from above to below  $E_F$  and the Dirac-like dispersion is clearly observed [Figs. 4b(ii), 4c (ii, iii)]. These observations can be well reproduced by our *ab initio* calculations (Fig. 4d) by introducing a chemical potential shift on the surface. Furthermore, the direct observations of the whole TDSSs unambiguously demonstrate the nontrivial bulk topology. In addition to the significant energy shift of the Dirac-like TSSs (Fig. 4g), a less-dramatic downward shift of bulk bands is revealed (as highlighted by the red dashed curves in Figs. 4e and 4f). In particular, the electron-like VHS1 band around the  $\Gamma$  point increase in size and its bottom drops by about 30 meV, as evidenced by the doping dependent energy distribution curve (EDC) taken at the  $\Gamma$  point (Fig. 4h). It is obvious that the distinct doping evolution of the Dirac bands (Figs. 4c and 4g) and VHS1 band (Fig. 4h) cannot be explained by a simple rigid band shift of the  $E_F$ , reflecting the different chemical potential changes of the surface and bulk states with doping, as confirmed by the calculations (Fig. 4d).

Our ARPES measurements, combined with DFT calculations, reveal the desired  $\mathbb{Z}_2$  TDSSs for the first time in a kagome metal, namely in the magnetic kagome metal  $\text{GdV}_6\text{Sn}_6$ . In addition, we identify multiple VHSs at the M point and demonstrate the successful manipulations of the TDSSs and VHSs by surface doping. With increasing doping, the Dirac point of the TDSSs is tuned from above to below  $E_F$ . Notably, upon sufficient doping, the lower branch of the TDSSs can merge into the bulk bands and only the upper branch crosses  $E_F$ , resulting in spin chirality reversal on the Fermi surfaces in  $\text{GdV}_6\text{Sn}_6$  [as illustrated in the inset of Fig. 4 d(iii), for details see Supplementary Figs. S8 and S9]. Such highly tunable TDSSs show great promise for controlling spin current via local electrostatic gates [tuning the Dirac point below the  $E_F$ , see the inset of Fig. 4d(iii)], which deserves further experimental investigation. Moreover, the revealed tunability of the VHSs holds the potential for realizing exotic correlated states on the surface of  $\text{GdV}_6\text{Sn}_6$  through Fermi surface nesting and sublattice interference by nonlocal interactions [27,30-33]. On the other hand, as  $\text{GdV}_6\text{Sn}_6$  trends to form magnetic ordering below the  $T_m$ , our results would stimulate future studies on the nontrivial states in magnetic phases. For instance, at low temperature, the magnetic Gd layers can become ferromagnetic by applying a weak magnetic field, which can gap out the surface Dirac cone and generate a nontrivial Chern number (see Supplementary Fig. S10 for the electronic structure of  $\text{GdV}_6\text{Sn}_6$  in ferromagnetism). This realizes a quantum anomalous Hall state on the surface of  $\text{GdV}_6\text{Sn}_6$  and the corresponding edge states and edge currents may be detected in a step edge in STM measurements, or in thin-film transport measurements. Therefore, these results establish the kagome metals  $\text{GdV}_6\text{Sn}_6$  as a fascinating playground for studying the nontrivial band topology intertwined with electronic correlation and magnetism.

## References

- [1] S. Nakatsuji, N. Kiyohara, and T. Higo. Large anomalous Hall effect in a non-collinear antiferromagnet at room temperature. *Nature* **527**, 212–215 (2015).
- [2] J.-X. Yin, S. S. Zhang, H. Li, K. Jiang, G. Chang, B. Zhang, B. Lian, C. Xiang, I. Belopolski, H. Zheng, T. A. Cochran, S.-Y. Xu, G. Bian, K. Liu, T.-R. Chang, H. Lin, Z.-Y. Lu, Z. Wang, S. Jia, W. Wang, and M. Z. Hasan, Giant and anisotropic many-body spin–orbit tunability in a strongly correlated kagome magnet. *Nature* **562**, 91–95 (2018).
- [3] L. Ye, M. Kang, J. Liu, F. Cube, C. R. Wicker, T. Suzuki, C. Jozwiak, A. Bostwick, E. Rotenberg, D. C. Bell, L. Fu, R. Comin, and Joseph G. Checkelsky, Massive Dirac fermions in a ferromagnetic kagome metal, *Nature* (London) **555**, 638–642 (2018).
- [4] E. Liu, Y. Sun, N. Kumar, L. Muechler, A. Sun, L. Jiao, S.-Y. Yang, D. Liu, A. Liang, Q. Xu, J. Kroder, V. Süß, H. Borrmann, C. Shekhar, Z. Wang, C. Xi, W. Wang, W. Schnelle, S. Wirth, Y. Chen, S. T. B. Goennenwein, and C. Felser, Giant anomalous Hall effect in a ferromagnetic kagome-lattice semimetal. *Nat. Phys.* **14**, 1125–1131 (2018).
- [5] J.-X. Yin, S. S. Zhang, G. Chang, Q. Wang, S. S. Tsirkin, Z. Guguchia, B. Lian, H. Zhou, K. Jiang, I. Belopolski, N. Shumiya, D. Multer, M. Litskevich, T. A. Cochran, H. Lin, Z. Wang, T. Neupert, S. Jia, H. Lei, and M. Z. Hasan, Negative flat band magnetism in a spin–orbit-coupled correlated kagome magnet, *Nat. Phys.* **15**, 443–448 (2019).
- [6] H. Tsai, T. Higo, K. Kondou, T. Nomoto, A. Sakai, A. Kobayashi, T. Nakano, K. Yakushiji, R. Arita, S. Miwa, et al., Electrical manipulation of a topological antiferromagnetic state, *Nature* **580**, 608–613 (2020).
- [7] M. Kang, L. Ye, S. Fang, J.-S. You, A. Levitan, M. Han, J. I. Facio, C. Jozwiak, A. Bostwick, E. Rotenberg, M. K. Chan, R. D. McDonald, D. Graf, K. Kaznatcheev, E. Vescovo, D. C. Bell, E. Kaxiras, J. Brink, M. Richter, M. P. Ghimire, J. G. Checkelsky, and R. Comin, Dirac fermions and flat bands in the ideal kagome metal  $\text{FeSn}$ , *Nat. Mater.* **19**, 163–169 (2020).
- [8] J.-X. Yin, W. Ma, T. A. Cochran, X. Xu, S. S. Zhang, H.-J. Tien, N. Shumiya, G. Cheng, K. Jiang, B. Lian, Z. Song, G. Chang, I. Belopolski, D. Multer, M. Litskevich, Z.-J. Cheng, X. P. Yang, B. Swidler, H. Zhou, H. Lin, T. Neupert, Z. Wang, N. Yao, T.-R. Chang, S. Jia, and M. Z. Hasan, Quantum-limit Chern topological magnetism in  $\text{TbMn}_6\text{Sn}_6$ , *Nature* (London) **583**, 533–536 (2020).
- [9] S.-Y. Yang, Y. Wang, B. R. Ortiz, D. Liu, J. Gayles, E. Derunova, R. Gonzalez-Hernandez, L. Smejkal, Y. Chen, S. S. P. Parkin, S. D. Wilson, E. S. Toberer, T. McQueen, and M. N. Ali, Giant, unconventional anomalous Hall effect in the metallic frustrated magnet candidate,  $\text{KV}_3\text{Sb}_5$ , *Sci. Adv.* **6**, abb6003 (2020).
- [10] Z. Liang, X. Hou, F. Zhang, W. Ma, P. Wu, Z. Zhang, F. Yu, J.-J. Ying, K. Jiang, L. Shan, Z. Wang, X.-H. Chen, Three-dimensional charge density wave and robust zero-bias conductance peak inside the superconducting vortex core of a kagome superconductor  $\text{CsV}_3\text{Sb}_5$ , *Phys. Rev. X* **11**, 031026 (2021).

- [11] N. Morali, R. Batabyal, P. K. Nag, E. Liu, Q. Xu, Y. Sun, B. Yan, C. Felser, N. Avraham, and H. Beidenkopf, Fermi-arc diversity on surface terminations of the magnetic Weyl semimetal  $\text{Co}_3\text{Sn}_2\text{S}_2$ , *Science* **365**, 1286–1291 (2019).
- [12] D.-F. Liu, A.-J. Liang, E.-K. Liu, Q.-N. Xu, Y.-W. Li, C. Chen, D. Pei, W.-J. Shi, S. K. Mo, P. Dudin, T. Kim, C. Cacho, G. Li, Y. Sun, L. X. Yang, Z. K. Liu, S. P. Parkin, C. Felser, Y. L. Chen, Magnetic Weyl semimetal phase in a Kagomé crystal, *Science* **365**, 1282–1285 (2019).
- [13] M. Li, Q. Wang, G. Wang, Z. Yuan, W. Song, R. Lou, Z. Liu, Y. Huang, Z. Liu, H. Lei, Z. Yin, and S. Wang, Spin-polarized Dirac cone, flat band and saddle point in kagome magnet  $\text{YMn}_6\text{Sn}_6$ , *Nat. Commun.* **12**, 3129 (2021).
- [14] N. J. Ghimire, R. L. Dally, L. Poudel, D. C. Jones, D. Michel, N. T. Magar, M. Bleuel, M. A. McGuire, J. S. Jiang, J. F. Mitchell, J. W. Lynn, and I. I. Mazin, Competing magnetic phases and fluctuation-driven scalar spin chirality in the kagome metal  $\text{YMn}_6\text{Sn}_6$ , *Sci. Adv.* **6**, 51 (2020).
- [15] W. Ma, X. Xu, J.-X. Yin, H. Yang, H. Zhou, Z.-J. Cheng, Y. Huang, Z. Qu, F. Wang, M. Z. Hasan, and S. Jia, Rare Earth Engineering in  $\text{RMn}_6\text{Sn}_6$  (R = Gd-Tm, Lu) Topological Kagome Magnets, *Phys. Rev. Lett.* **126**, 246602 (2021)
- [16] B. R. Ortiz, S. M. Teicher, Y. Hu, J. L. Zuo, P. M. Sarte, E. C. Schueller, A. M. Abeykoon, M. J. Krogstad, S. Rosenkranz, R. Osborn, R. Seshadri, L. Balents, J. He, and S. D. Wilson,  $\text{CsV}_3\text{Sb}_5$ : A  $\mathbb{Z}_2$  Topological Kagome Metal with a Superconducting Ground State, *Phys. Rev. Lett.* **125**, 247002 (2020).
- [17] H. Chen, B. Hu, Z. Zhao, J. Yuan, Y. Xing, G. Qian, Z. Huang, G. Li, Y. Ye, Q. Yin, C. Gong, Z. Tu, H. Lei, S. Ma, H. Zhang, S. Ni, H. Tan, C. Shen, X. Dong, B. Yan, Z. Wang, and H. -J. Gao, Roton pair density wave and unconventional strong-coupling superconductivity in a topological kagome metal, *Nature* **559**, 222–228(2021).
- [18] H. Zhao, H. Li, B. R. Ortiz, S. M. L. Teicher, T. Park, M. Ye, Z. Wang, L. Balents, S. D. Wilson, and I. Zeljkovic, Cascade of correlated electron states in a kagome superconductor  $\text{CsV}_3\text{Sb}_5$ , *Nature* **599**, 216–221 (2021).
- [19] M. G. Kang, S. Fang, J. Kim, B. R. Ortiz, S. H. Ryu, J. Kim, J. Yoo, G. Sangiovanni, D. D. Sante, B.-G. Park, C. Jozwiak, A. Bostwick, E. Rotenberg, E. Kaxiras, S. D. Wilson, J.-H. Park, and Riccardo Comin, Twofold van Hove singularity and origin of charge order in topological kagome superconductor  $\text{CsV}_3\text{Sb}_5$ . Preprint at arXiv:2105.01689 (2021).
- [20] Y. Hu, X. Wu, B. R. Ortiz, S. Ju, X. Han, J. Z. Ma, N. C. Plumb, M. Radovic, R. Thomale, S. D. Wilson, A. P. Schnyder, and M. Shi, Rich nature of van Hove singularities in kagome superconductor  $\text{CsV}_3\text{Sb}_5$ , Preprint at arXiv:2106.05922 (2021).
- [21] Y.-X. Jiang, J.-X. Yin, M. M. Denner, N. Shumiya, B. R. Ortiz, J. He, X.-X. Liu, S.-T. S. Zhang, G.-Q. Chang, I. Belopolski, Q. Zhang, T. A. Cochran, D. Multer, M. Litskevich, Z.-J. Cheng, X. P. Yang, Z. Wang, R. Thomale, T. Neupert, S. D. Wilson, and M. Zahid Hasan, Unconventional chiral charge order in kagome superconductor  $\text{KV}_3\text{Sb}_5$ , *Nat. Mater.* **20**, 1353–1357 (2021).
- [22] C. Mielke III, D. Das, J.-X. Yin, H. Liu, R. Gupta, C. N. Wang, Y.-X. Jiang, M. Medarde, X. Wu, H. C. Lei, J. J. Chang, P. Dai, Q. Si, H. Miao, R. Thomale, T. Neupert, Y. Shi, R. Khasanov, M. Z. Hasan, H. Luetkens, and Z. Guguchia, Time-reversal symmetry-breaking charge order in a correlated kagome superconductor, Preprint at arXiv:2106.13443 (2021).
- [23] Z. Hao, Y. Cai, Y. Liu, Y. Wang, X. Sui, X.-M. Ma, Z. Shen, Z. Jiang, Y. Yang, W. Liu, Q. Jiang, Z. Liu, M. Ye, D. Shen, Y. Liu, S. Cui, J. Chen, L. Wang, C. Liu, J. Lin, J. Wang, B. Huang, J.-W. Mei, and C. Chen, Dirac Nodal Lines and Nodal Loops in a Topological Kagome Superconductor  $\text{CsV}_3\text{Sb}_5$ , Preprint at arXiv:2111.02639 (2021).
- [24] Y. Hu, S. M. L. Teicher, B. R. Ortiz, Y. Luo, S. Peng, L. Huai, J. Z. Ma, N. C. Plumb, S. D. Wilson, J.-F. He, and M. Shi, Charge-order-assisted topological surface states and flat bands in the kagome superconductor  $\text{CsV}_3\text{Sb}_5$ , Preprint at arXiv:2104.12725 (2021).
- [25] G. Pokharel, S. M. L. Teicher, B. R. Ortiz, P. M. Sarte, G. Wu, S. Peng, J. He, R. Seshadri, and S. D. Wilson, Electronic properties of the topological kagome metals  $\text{YV}_6\text{Sn}_6$  and  $\text{GdV}_6\text{Sn}_6$ , *Phys. Rev. B* **104**, 235139 (2021).
- [26] H. Ishikawa, T. Yajima, M. Kawamura, H. Mitamura, and K. Kindo,  $\text{GdV}_6\text{Sn}_6$ : A Multi-carrier Metal with Non-magnetic 3d-electron Kagome Bands and 4f-electron Magnetism, *J. Phys. Soc. Jpn.* **90**, 124704 (2021).
- [27] X. Wu, T. Schwemmer, T. Müller, A. Consiglio, G. Sangiovanni, D. D. Sante, Y. Iqbal, W. Hanke, A. P. Schnyder, M. M. Denner, M. H. Fischer, T. Neupert, and R. Thomale, Nature of unconventional pairing in the kagome superconductors  $\text{AV}_3\text{Sb}_5$ , *Phys. Rev. Lett.* **127**, 177001 (2021).
- [28] C.-K. Chiu, J. C. Y. Teo, A. P. Schnyder, and S. Ryu, Classification of topological quantum matter with symmetries, *Rev. Mod. Phys.* **88**, 035005 (2016).
- [29] S. Peng, Y. Han, G. Pokharel, J. Shen, Z. Li, M. Hashimoto, D. Lu, B. R. Ortiz, Y. Luo, H. Li, M. Guo, B. Wang, S. Cui, Z. Sun, Z. Qiao, S. D. Wilson, and J. He, Realizing Kagome Band Structure in Two-Dimensional Kagome Surface States of  $\text{RV}_6\text{Sn}_6$  (R=Gd,Ho), *Phys. Rev. Lett.* **127**, 266401 (2021).
- [30] M. L. Kiesel, and R. Thomale, Sublattice interference in the kagome Hubbard model, *Phys. Rev. B* **86**, 121105(R) (2012).
- [31] M. L. Kiesel, C. Platt, and R. Thomale, Unconventional Fermi Surface Instabilities in the Kagome Hubbard Model, *Phys. Rev. Lett.* **110**, 126405 (2013).
- [32] W.-S. Wang, Z.-Z. Li, Y.-Y. Xiang, and Q.-H. Wang, Competing electronic orders on kagome lattices at van Hove filling, *Phys. Rev. B* **87**, 115135 (2013).

- [33] S. Xu, M. M. A. Ezzi, N. Balakrishnan, A. Garcia-Ruiz, B. Tsim, C. Mullan, J. Barrier, N. Xin, B. A. Piot, T. Taniguchi, K. Watanabe, A. Carvalho, A. Mishchenko, A. K. Geim, V. I. Fal'ko, S. Adam, A. H. Castro Neto, K. S. Novoselov, and Y. Shi, Tunable van Hove singularities and correlated states in twisted monolayer–bilayer graphene, *Nat. Phys.* **17**, 619–626 (2021).
- [34] P. Giannozzi, S. Baroni, N. Bonini, M. Calandra, R. Car, C. Cavazzoni, D. Ceresoli, G. L. Chiarotti, M. Cococcioni, and I. Dabo, QUANTUM ESPRESSO: a modular and open-source software project for quantum simulations of materials, *J. Phys. Condens. Matter* **21**, 395502 (2009).
- [35] J. P. Perdew, K. Burke, and M. Ernzerhof, Generalized Gradient Approximation Made Simple, *Phys. Rev. Lett.* **77**, 3865 (1996).
- [36] A. A. Mostofi, J. R. Yates, G. Pizzi, Y.-S. Lee, I. Souza, D. Vanderbilt, and N. Marzari, An updated version of wannier90: A tool for obtaining maximally-localised Wannier functions, *Comput. Phys. Commun.* **185**, 2309–2310 (2014).
- [37] M. P. Lopez Sancho, J. M. Lopez Sancho, J. M. L. Sancho, and J. Rubio, Highly convergent schemes for the calculation of bulk and surface Green functions, *J. Phys. F: Met. Phys.* **15**, 851 (1985).

## Methods

**Sample growth** Single crystals of  $\text{GdV}_6\text{Sn}_6$  were grown from the Sn-flux with the loading composition of  $\text{Gd}:\text{V}:\text{Sn} = 1:6:20$ . The sample was heated up to  $1050\text{ }^\circ\text{C}$  and stay at  $1050\text{ }^\circ\text{C}$  for 10 hours, then slowly cooled down to  $650\text{ }^\circ\text{C}$  at the speed of  $3\text{ }^\circ\text{C}/\text{hour}$ . The extra Sn flux was centrifuged at  $650\text{ }^\circ\text{C}$ . The grown single crystals were carefully examined by single crystal X-ray diffraction to obtain the accurate lattice parameters and atomic coordinates. Accordingly,  $\text{GdV}_6\text{Sn}_6$  crystallizes in a layered structure with the space group  $P6/mmm$ .

**ARPES measurements** The  $\text{GdV}_6\text{Sn}_6$  samples were cleaved *in-situ* with a base pressure of better than  $5 \times 10^{-11}$  torr. Angle-resolved photoemission (ARPES) measurements were performed at the ULTRA endstation of the Surface/Interface Spectroscopy (SIS) beamline of the Swiss Light Source using a Scienta-Omicron DA30L analyzer. The temperature was 20 K, and total energy resolution was better than  $15\text{ meV}$ . The Fermi level was determined by measuring a polycrystalline Au in electrical contact with the samples.

**DFT calculations** Band structure calculations were performed by using the method of first-principles density functional theory (DFT) as implemented in the QUANTUM ESPRESSO (QE) code [34]. The cutoff energy for expanding the wave functions into a planewave basis was set to 60 Ry and the adopted K-point grid is  $9 \times 9 \times 5$ . The exchange correlation energy was described by the generalized gradient approximation (GGA) using the PBE functional [35]. The calculations were done for nonmagnetic  $\text{GdV}_6\text{Sn}_6$  with spin-orbit coupling. We used the maximally localized Wannier functions (MLWFs) to construct a tight-binding model by fitting the DFT band structure, where 118 MLWFs were included ( $\text{Gd } d, \text{V } d, \text{Sn } s, p_x$ ) [36] and then we used the surface state Green's function method to calculate topological surface states [37]. For all calculations, we used the experimentally determined crystal structure and lattice constants ( $a = 5.5348\text{ \AA}$  and  $c = 9.1797\text{ \AA}$ ).

## Declarations

### Acknowledgements

The work at PSI was supported by the Swiss National Science Foundation under Grant. No. 200021-188413, the Sino-Swiss Science and Technology Cooperation (Grant No. IZLCZ2-170075). Y.H. was supported by the National Natural Science Foundation of China (12004363). J.Z.M. was supported by the National Natural Science Foundation of China (12104379), Guangdong Basic and Applied Basic Research Foundation (2021B1515130007). The work at Rutgers was supported by U.S. DOE-BES under Contract DE-SC0022156.

### Author Contributions

Y.H. and J.-Z.M. designed the research. Y.Y. grew and characterized the crystals with guidance from W.X.. X.W. performed the theoretical calculations with the support from A.P.S.. Y.H. and J.Z.M. performed the ARPES experiments with help from N.C.P. and M.S.. Y.H. analyzed the data and discussed with J.Z.M. and M.S.. Y.H. draw the figures with help from X.W. and J.Z.M.. Y.H. wrote the paper with inputs from J.M. and X.W.. All authors contributed to the discussions. M.S., J.Z.M. and Y.H. supervised the project.

### Data availability

The data that support the findings of this study are available from the corresponding authors upon reasonable request.

## Figures

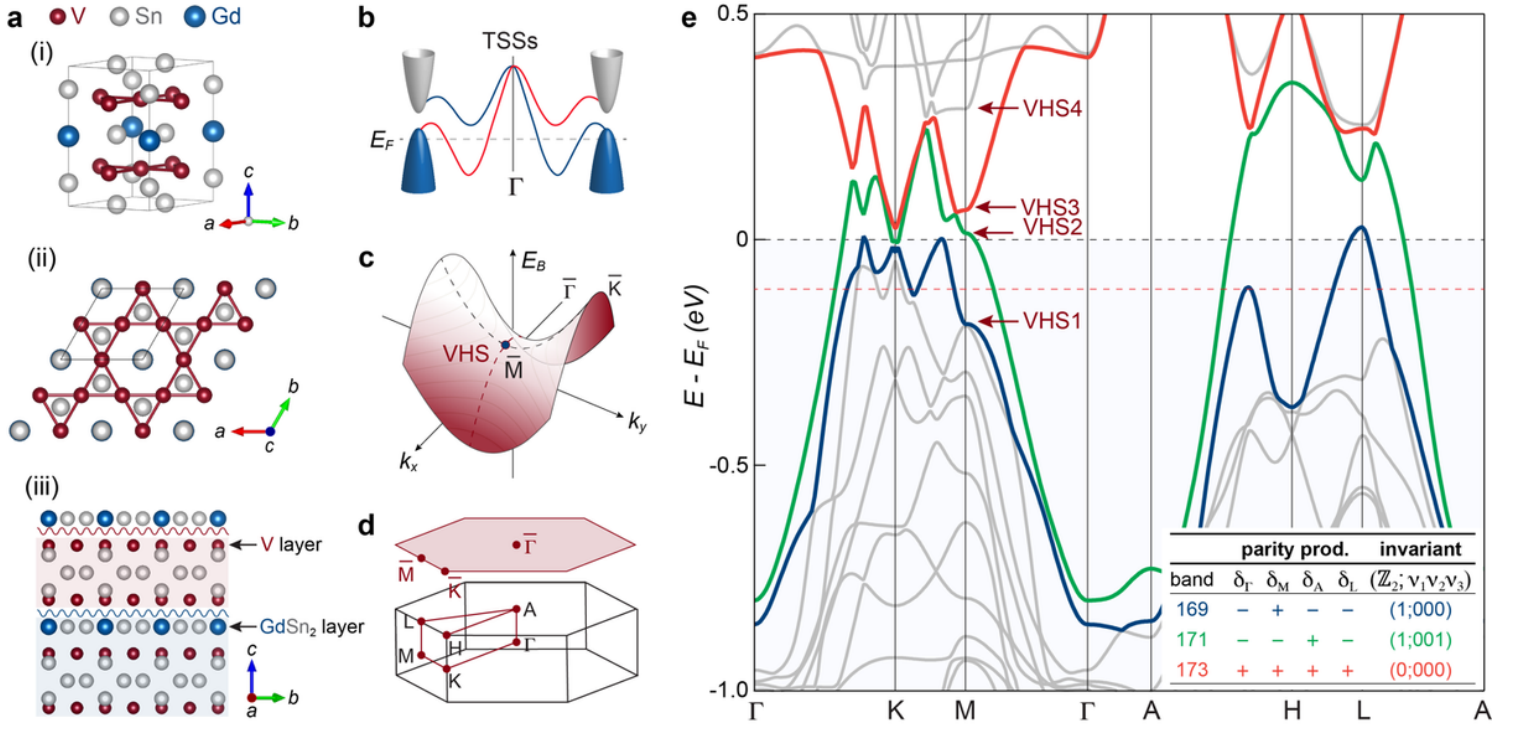


**Figure 1**  
**Crystal structure, topological classification, and van Hove singularities in kagome metals  $GdV_6Sn_6$ .** **a** Crystal structure of  $GdV_6Sn_6$  showing the unit cell (i), top view looking along the  $c$  axis and showing the V kagome plane (ii), side view showing two possible surface terminations as indicated by wavy line (iii). **b** Sketch of topologically nontrivial states (TSSs) in  $GdV_6Sn_6$ . Cones and curves represent bulk states and TSSs, respectively. **c** Schematic of a van Hove singularity (VHS) in a two-dimensional electron system. **d** Bulk Brillouin zone (BZ) of  $GdV_6Sn_6$  and the projection of the (001) surface BZ, with high symmetry points marked. **e** Density functional theory calculated electronic structure of  $GdV_6Sn_6$ . The red dashed line indicates the Fermi level suggested by the ARPES measurement. The inset shows the parity products classifying the  $\mathbb{Z}_2$  invariant for each band. Bands 169 (blue) and 171 (green) are characterized by a strong topological invariant,  $\mathbb{Z}_2 = 1$ , while band 173 (red) is trivial with no topological invariants.

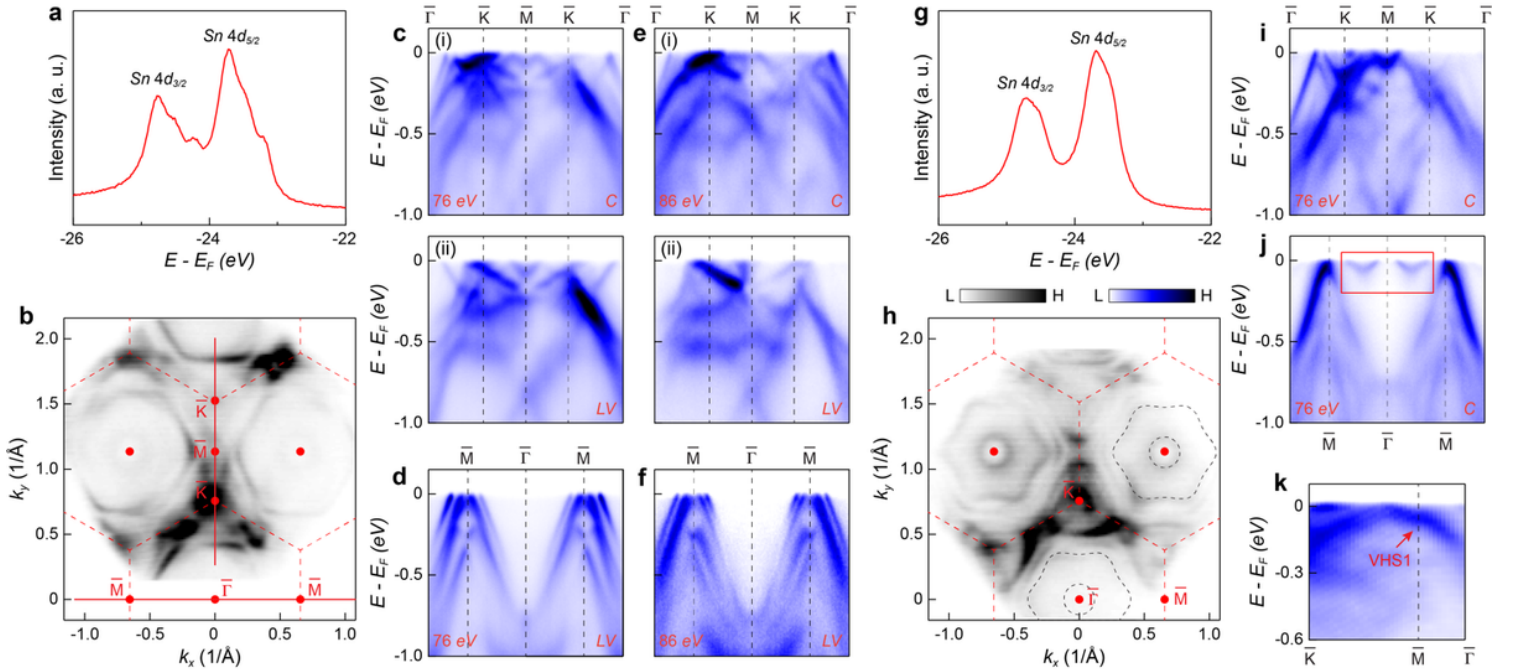


**Figure 2**  
**Termination dependence of the electronic structure in  $GdV_6Sn_6$ .** **a** XPS spectrum of *in situ* freshly cleaved  $GdV_6Sn_6$ , from which we suggest that the surface termination is the kagome layer (see Supplementary Fig. S3). **b** Fermi surface mapping measured on the kagome termination. The BZ is marked with the red dashed hexagon. **c** ARPES spectrum taken along the  $G-K$  direction on the kagome termination, measured with 76 eV circular (C) (i) and linear vertical (LV) (ii) polarization. **d** and **e** show similar ARPES spectra for the kagome termination. **f** shows the Fermi surface mapping for the kagome termination. **g** XPS spectrum of *in situ* freshly cleaved  $GdV_6Sn_6$ , from which we suggest that the surface termination is the Sn layer (see Supplementary Fig. S3). **h** Fermi surface mapping measured on the Sn termination. The BZ is marked with the red dashed hexagon. **i** and **j** show ARPES spectra taken along the  $G-K$  direction on the Sn termination, measured with 76 eV circular (C) (i) and linear vertical (LV) (ii) polarization. **k** shows the Fermi surface mapping for the Sn termination. **VHS1** is indicated by a red arrow.

polarized light. The momentum path is indicated by the red solid line in (b). **d** Same as (c), but taken along the  $G - M$  direction, and measured with  $LV$  polarization. **e, f** Same as (c, d), but probed with 86 eV photons. **g, h** Same as (a, b), but measured on the  $GdSn_2$  termination. The black dashed curve marks the electronic pocket. **i, j** Same as (c, d), but measured with  $C$  polarization on the  $GdSn_2$  termination. **k** Band dispersion along the  $K - M - G$  path  $\in gtheVHS1$  at the  $M$  point.

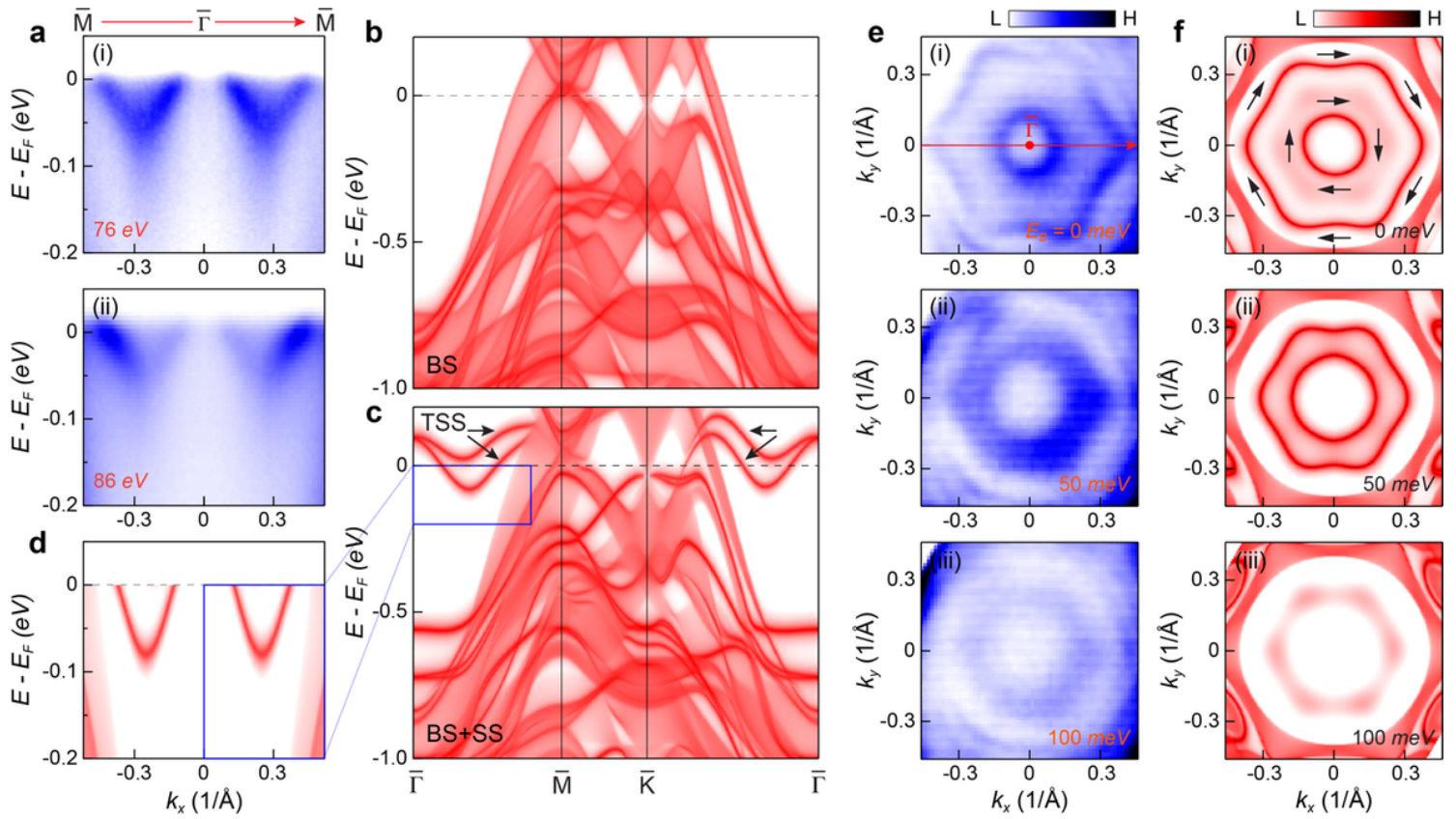


**Figure 3**

**$Z_2$  Topological surface states in  $GdV_6Sn_6$ .** **a** Photon energy-dependent ARPES spectra taken along the  $G - M$  direction, measured with 76 eV (i) and 86 eV (ii). **b, c** The (001) surface Green's function projection of pure bulk states (BS) (b) and the states [BS and surface states (SS)] on  $GdSn_2$  termination (c). **d** Zoom-in plot of the calculated TSSs with the same energy-momentum range as the experimental dispersions in (a). **e, f** Side-by-side comparison between experiments (e) and calculations (f), which exhibits excellent agreement, of three representative constant-energy contours ( $E_B = 0, 50, 100$  meV). The black arrows in (f) indicate the spin texture of the TSSs.

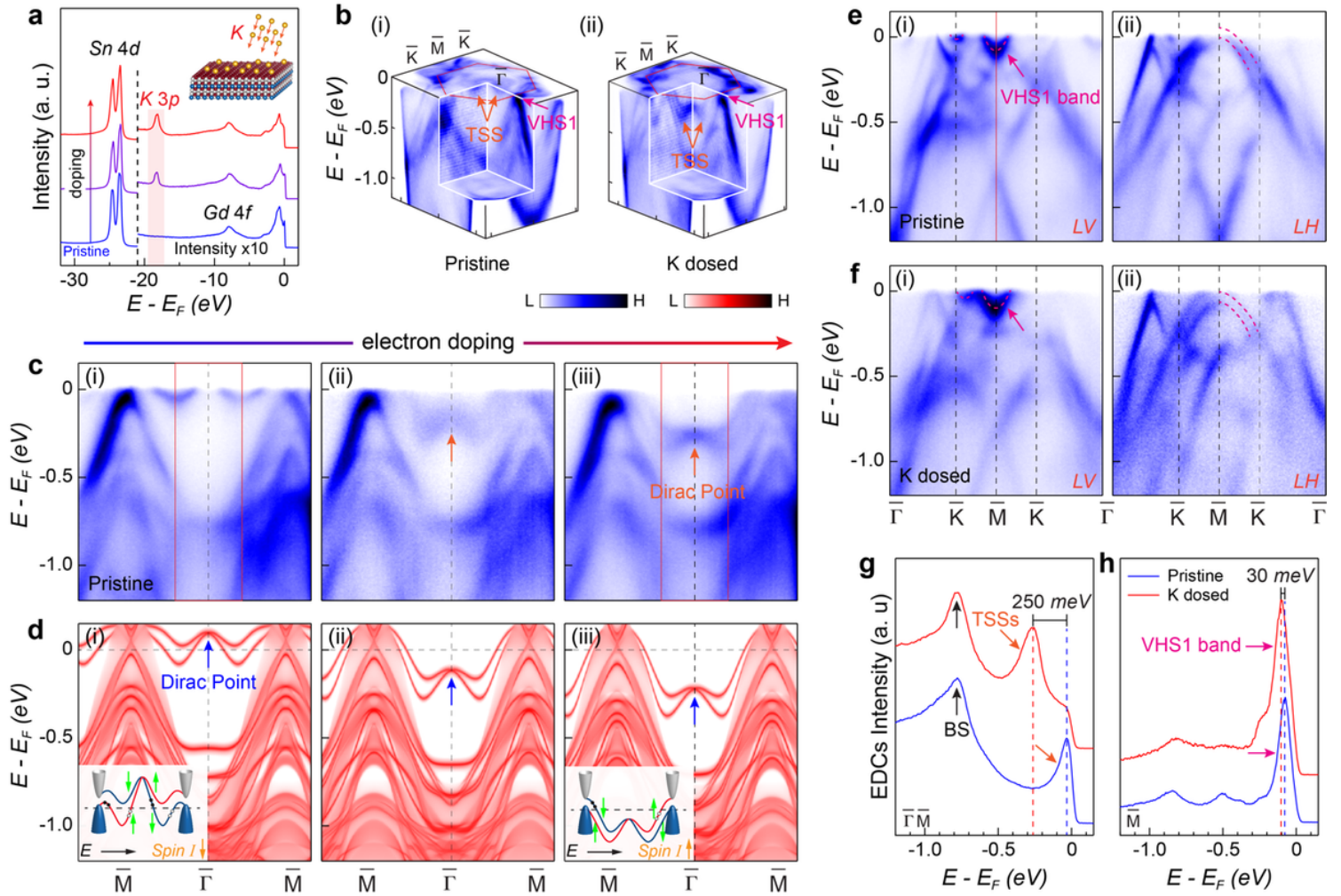


**Figure 4**

**Manipulation of the TSSs and VHS via *in-situ* potassium deposition.** **a** Doping dependence of the XPS spectrum recorded on the  $\text{GdSn}_2$  termination, showing the characteristic Sn 4d and Gd 4f peaks. Upon potassium deposition, the K 3p peak emerges (purple and red curves), which is absent on the pristine surface (blue curve). **b** 3D intensity plot of the electronic structure measured on the pristine (i) and K dosed surfaces (ii). The orange arrow highlights the TSSs. **b, c** Doping evolution of the band structure along the  $G - M$  direction from experiments (c) and calculations (d). The Dirac cone of the TSSs is above the Fermi level ( $E_F$ ) before doping (pristine, i) and is tuned below  $E_F$  with electron doping (ii, iii). The arrows indicate the Dirac cone of the TSSs. The insets in [d(i)] and [d(iii)] show the schematic of distinct spin current of TDSSs without and with doping. **e** ARPES spectra taken along the  $G - K$  direction, on the pristine surface ( $\text{GdSn}_2$  termination), measured with 76 eV LV (i) and linear horizontal (LH) (ii) polarizations. Red dashed curve highlights bulk bands. The arrow indicates the VHS1 band. **f** Same as (e), but measured on the K dosed surface. **g** Doping evolution of the integrated energy distribution curve (EDC) taken around  $\Gamma$ . The integration window of the EDC is represented by the red box in [c(i)] and [c(iii)]. Red and black arrows mark the TSSs and BS, respectively. **h** Doping evolution of the EDC extracted at the  $M$  point, as indicated by the red line in [e(i)].

## Supplementary Files

This is a list of supplementary files associated with this preprint. Click to download.

- [SupplementaryMaterials.docx](#)